

1

2 **Dynamical Downscaling of Future Hydrographic Changes**
3 **over the Northwest Atlantic Ocean**

4 Sang-Ik Shin^{1,2,*} and Michael A. Alexander²

5 ¹ CIRES, University of Colorado, Boulder, CO.

6 ² Physical Science Division, NOAA Earth System Research Laboratory, Boulder, CO.

7

8 will be submitted to *Journal of Climate*

9 (July 1, 2019)

10

* Corresponding author address: Sang-Ik Shin, NOAA/ESRL, 325 Broadway, R/PSD1, Boulder, CO 80305.

E-mail: Sangik.Shin@noaa.gov

11 **Abstract**

12 Projected climate changes along the U.S. East and Gulf Coasts were examined
13 using the eddy-resolving Regional Ocean Modeling System (ROMS). First, a control
14 (CTRL) ROMS simulation was performed using boundary conditions derived from
15 observations. Then climate change signals, obtained as mean seasonal cycle differences
16 between the recent past (1976-2005) and future (2070-2099) periods in a coupled global
17 climate model under the RCP8.5 greenhouse gas trajectory, were added to the initial and
18 boundary conditions of the CTRL in a second (RCP85) ROMS simulation. The difference
19 between the RCP85 and CTRL simulations were used to investigate the regional effects of
20 climate change.

21 Relative to the coarse resolution coupled climate model, the downscaled projection
22 shows that SST changes become more pronounced near the U.S. East Coast, and the Gulf
23 Stream is further reduced and shifted southward. Moreover, the downscaled projection
24 shows enhanced warming of ocean bottom temperatures along the U.S. East and Gulf
25 Coasts, particularly in the Gulf of Maine and the Gulf of Saint Lawrence. The enhanced
26 warming was related to an improved representation of the ocean circulation, including
27 topographically trapped coastal ocean currents and slope water intrusion through the
28 Northeast Channel into the Gulf of Maine. In response to increased radiative forcing, much
29 warmer than present-day Labrador Subarctic slope waters entered the Gulf of Maine
30 through the Northeast Channel warming the deeper portions of the Gulf by more than 4°C.

31

32 1. Introduction

33 Projections of future ocean conditions are often requested for long term planning
34 and management of marine resources. These projections require sustained observations of
35 the system as well as a modeling framework that represents the relevant ocean processes
36 and feedbacks with other systems (e.g. atmosphere, ice, land, biogeochemistry, etc.) to
37 resolve the mechanisms important to variability of the system. In this regard, projections
38 from simulations participating in Phase 5 of the Coupled Climate Model Intercomparison
39 Project (CMIP5; [Taylor et al. 2012](#)) provide physically consistent estimates of climate
40 change over the northwest Atlantic, since those simulations include state-of-the-art ocean
41 processes and feedbacks among subsystems. However, CMIP5 models have several
42 intrinsic shortcomings, including coarse horizontal resolution, on the order of 1° in the
43 midlatitude oceans, and a limited number of vertical ocean layers. Moreover, errors in
44 coupled climate models are not uniformly distributed over the globe; for example, sea
45 surface temperature (SST) errors are generally largest along the continental margins (e.g.
46 Fig. 3 in [He and Soden 2016](#)).

47 How can we improve climate projections for coastal oceans? One approach is to
48 use a high-resolution coupled climate model. Climate models with very high resolution
49 (~10 km) in the ocean component used by [Small et al. \(2014\)](#), [Griffies et al. \(2015\)](#) and
50 [Saba et al. \(2016\)](#) were successful in reproducing many aspects of the ocean state and in
51 reducing biases in the coastal oceans, including the northeast U.S. coast. However, the
52 current generation of high-resolution coupled climate models still have substantial mean

53 biases. For example, the cold SST bias in the central North Atlantic remains and can exceed
54 5 °C in some high-resolution models (e.g. Fig. 2 in [Saba et al. 2016](#)).

55 On the other hand, previous studies have shown that uncoupled regional ocean
56 models, employing a high-resolution grid in both horizontal and vertical directions,
57 improve many aspects of ocean processes along continental margins, including
58 topographically trapped coastal currents, eddies, tidal mixing, river plumes, etc. Regional
59 models have been especially useful in simulating ocean processes along the U.S. East Coast
60 and Gulf of Mexico (e.g. [Curchitser et al. 2005](#); [Kang and Curchitser 2013](#); [Kang and](#)
61 [Curchitser 2015](#)) and for shelf and bays in the Gulf of Mexico and Atlantic seaboard ([Liu](#)
62 [et al. 2012](#); [Alexander 2019](#)), due to their complex coastlines, highly variable bathymetry,
63 and proximity to strong coastal currents. Regional ocean models can be used to investigate
64 climate change by forcing them with bias-adjusted future projections from global models.
65 This has generally been done using the “delta method”, where long-term mean differences
66 in oceanic and atmospheric fields between the recent past and future periods were derived
67 from coupled climate models, and then added to the observed present-day conditions. By
68 design, this approach only considers the effects of the long-term climate change (forced)
69 signal and neglects the somewhat uncertain future projections at higher frequencies, such
70 as changes in storm tracks and interannual climate variability.

71 Differences between low-resolution coupled and high-resolution regional models
72 are illustrated in [Fig. 1](#), which shows the wintertime temperature and circulation patterns
73 along the northeast U.S. shelf (see [Fig. S1](#) of Supplementary Information for the
74 summertime). The fields are obtained from the Geophysical Fluid Dynamics Laboratory

75 (GFDL) Earth System Model that includes ocean biogeochemistry, the GFDL-ESM2M
76 (Dunne et al. 2012), and 7-km Regional Ocean Modeling System (ROMS) (see section 2a
77 for details). For example, at the surface ROMS exhibits a southeastward directed coastal
78 current along Nova Scotia that flows counterclockwise around the Gulf of Maine (see the
79 schematics in Fig. 2). These currents are weak or absent in the climate model. As observed,
80 cold SSTs ($< 7^{\circ}\text{C}$) extend over the entire Gulf of Maine in ROMS, but they occur only in
81 the very northern part of the Gulf in GFDL-ESM2M. At a 155 m depth, ROMS clearly
82 shows the intrusion of slope waters into the Gulf of Maine through the Northeast Channel
83 as in observations (e.g. Brooks 1987). The slope waters are a deep-water mass, consisting
84 of Labrador Slope Water and Warm Slope Water, and recognized as the major source of
85 dissolved inorganic nutrients to the Gulf (e.g. Townsend et al. 2014; Townsend et al. 2015).
86 The Gulf of Maine, including the northeast Channel, are not resolved in GFDL-ESM2M.

87 A more detailed examination of changes in the Gulf of Maine is warranted given
88 that it has very complex bathymetry and that it is near the confluence of the cold Labrador
89 Current and warm Gulf Stream (see Fig. 2). It has also experienced very strong warming
90 over the recent past (e.g. Pershing et al. 2015) that is projected to continue into the future
91 (e.g. Saba et al. 2015). The rapidly warming temperatures and accompanying changes in
92 currents and biogeochemistry will strongly impact marine ecosystems along the northeast
93 U.S. coast, (e.g. Heogh-Guldberg and Bruno 2010), with adverse effects on species such
94 as Atlantic cod (e.g. Pershing et al. 2015) and lobster (Le Bris et al. 2017).

95 In this study, we are interested in downscaling the future coastal ocean climate
96 under the Representative Concentration Pathway (RCP) 8.5 scenario. Here, we extend the

97 previous one-way nested regional ocean model approach by retaining the “mean seasonal
98 cycle” of the delta forcing fields. Recently, Alexander et al. (2019) provided a general
99 survey of such downscaled future coastal ocean climate under the RCP 8.5 scenario using
100 three CMIP5 participating coupled climate models, and here we performed a detailed
101 analysis of the one driven by the GFDL-ESM2M. This paper is organized as follows; a
102 summary of the models and methods are given in section 2; the results of downscaled ocean
103 climate changes over the entire model domain are summarized in section 3; a detailed
104 assessment of the changes in the Gulf of Maine are given in section 4; and the summary
105 and concluding remarks follow in section 5.

106

107 **2. Models and methods**

108 We first used ROMS to perform a control simulation (hereafter CTRL) of the recent
109 past along the U.S. East and Gulf Coasts. The large-scale projected changes (i.e. deltas)
110 were obtained from the GFDL-ESM2M simulations of historical and future periods. Then,
111 these delta fields were added to the initial and boundary conditions of the CTRL in a second
112 ROMS simulation (hereafter RCP85). A brief description of ROMS, the GFDL-ESM2M
113 simulations used, and delta method are given below.

114 *a. Regional ocean model*

115 Our study uses ROMS ([Schepetkin and McWilliams 2005](#)), a sigma-coordinate
116 primitive equation ocean model, with the same domain and physics as in [Kang and](#)
117 [Curchitser \(2013\)](#). The model domain covers the Northwest Atlantic Ocean and Gulf of

118 Mexico (hereafter NWA; see [Fig. 2](#)) with a horizontal resolution of 7 km and 40 vertical
119 terrain-following levels. For the CTRL simulation, initial and ocean lateral boundary
120 conditions (BCs) were derived from the Simple Ocean Data Assimilation ([SODA; Carton
121 and Giese 2008](#)) version 2.1.6, air-sea fluxes were calculated from the surface atmospheric
122 forcing fields extracted from the Coordinated Ocean-ice Reference Experiments (CORE)
123 version 2 data set ([Large and Yeager 2009](#)), and river discharge was implemented as a fresh
124 water flux using the global river flow and continental discharges database ([Dai et al. 2009](#)).
125 A more detailed description of the model physics is given in [Kang and Curchitser \(2013\)](#).

126 The CTRL was very successful in simulating many aspects of present-day climate
127 conditions over the NWA as discussed in [Kang and Curchitser \(2013\)](#). In [Fig. 3](#), we
128 compared the climatological annual mean surface currents derived from the CTRL (during
129 the yrs. 1976-2005) to the satellite-tracked surface drifting buoy (during the yrs. 1979-
130 2015; [Lumpkin and Johnson 2013](#)) and the SODA data set (during the period yrs. 1976-
131 2005). Despite the difference in time averaging periods and the uncertainties of model and
132 Lagrangian drifter data, the CTRL captures the observed circulation patterns in the NWA,
133 including the observed clockwise shelf circulation in the Gulf Mexico. Such coastal
134 circulation was not resolved in the relatively low-resolution SODA reanalysis. The SODA
135 reanalysis has a horizontal resolution of about 0.25° latitude x 0.4° longitude with 40
136 vertical levels (Note that the SODA had less than 15 vertical levels at the coastal ocean
137 where depth is shallower than 200 m). The Gulf Stream in CTRL, however, shows an
138 exaggerated split into two branches over the regions between 65°-55°W, though the drifter
139 also indicates some hints of this split.

140 *b. Coupled global climate model simulations*

141 The coupled climate model simulations used in this study are the historical (yrs.
142 1976-2005) and the RCP 8.5 (yrs. 2070-2099) simulations from the GFDL-ESM2M. The
143 atmospheric component, the Atmospheric Model version 2 (AM2; [Anderson et al. 2004](#)),
144 has a horizontal resolution of 2° latitude x 2.5° longitude with 24 vertical levels. The ocean
145 component, MOM4p1 ([Griffies et al. 2005](#)), has ~1° horizontal resolution with 50 vertical
146 levels. The horizontal resolution of the ocean component decreases to 1/3° meridionally at
147 the equator and uses tripolar grid north of 65°N. A detailed description of model physics is
148 given by [Dunne et al. \(2012\)](#).

149 The historical run is designed to simulate the recent past (yrs. 1850-2005) by
150 imposing observed radiative forcing changes due to natural (e.g. volcanoes) and
151 anthropogenic influences. The RCP 8.5 scenario, the projection with the greatest increase
152 in greenhouse gasses in CMIP5, starts in 2006 with the level of radiative forcing reaching
153 8.5 W m⁻² by 2100. The atmospheric CO₂ rises from 354.14 ppm (average of yrs. 1976-
154 2005) to 798.51 ppm (average of yrs. 2070-2099), although other trace gases contribute to
155 the radiative forcing. The increase in radiative forcing under the RCP 8.5 scenario causes
156 the global surface temperature to rise by 2-5 °C at the end of 21st century relative to 1986-
157 2005 average depending on which climate model is used ([IPCC 2013](#)). In GFDL-ESM2M,
158 the projected change is about 4.5°C.

159 Many previous studies (e.g. [Cheng et al. 2013](#)) found that the increase in radiative
160 forcing weakens the Atlantic Meridional Overturning Circulation (AMOC). In the GFDL-
161 ESM2M model simulations, AMOC decreases by about 20 % (~ 4 Sv; 1 Sv = 10⁶ m³ s⁻¹)

162 from the current climate conditions (~ 20 Sv; figure not shown). The projected regional
163 climate changes over the North Atlantic in GFDL-ESM2M are largely consistent with the
164 climate responses to reduced AMOC. For example, a large ocean surface warming along
165 the northeast coast of the U.S that extends into the central North Atlantic and a moderate
166 warming or even a small cooling over the subpolar North Atlantic (Fig. 4a) are consistent
167 with the fingerprint pattern for reduced AMOC (e.g. Cheng et al. 2013; Buckley and
168 Marshall 2016; Caesar et al. 2018). The subtropical North Atlantic is projected to be saltier
169 than in the present-day (Fig. 4b), in contrast to the projected fresher subpolar North
170 Atlantic. These surface temperature and salinity responses are also consistent with the
171 projected slow-down of Gulf Stream (Fig. 4c) that decreases meridional oceanic heat and
172 salt transport. The ocean bottom temperatures along the East Coast of North America show
173 2-3°C year-round warming (Fig. 5), which is somewhat larger than at the surface (Fig. 4a),
174 suggesting substantial changes in ocean stratification.

175 *c. Seasonally varying delta method*

176 To produce a high-resolution, bias-adjusted future projection for the NWA, we
177 dynamically downscale the ocean climate by using the delta method to obtain initial
178 conditions and boundary conditions including the surface atmospheric fluxes. The delta
179 approach has been used previously in many coastal ocean downscaling simulations (e.g.
180 Auad et al. 2006; Liu et al. 2012; van Hooidek et al. 2015). In those studies, the long-term
181 (typically 10-30 year) annual mean difference in BCs and surface atmospheric forcings
182 between the recent past and future periods were derived from coupled climate models, and
183 then added to the observed present-day conditions. This method does remove the mean

184 bias for the present-day climate of the coupled climate models, but also retains high-
185 frequency spatiotemporal variability of the forcings (i.e. the day-to-day variability and fine-
186 scale spatial variability of the present-day climate). The delta method, however, neglects
187 the changes in interannual climate variability due to an increase in greenhouse gases.

188 Here we extended the delta approach by retaining its seasonal cycle, given that
189 climate change signals often show a strong seasonal dependence ([Partanen et al. 2017](#); also
190 see our [Fig. 7](#)). The detailed procedure of estimating the seasonally varying delta is as
191 follows:

- 192 1) The monthly mean GFDL ESM2M simulated surface atmospheric ([Table 1](#)),
193 oceanic (sea surface height, 3-dimensional temperature, salinity, and currents), and
194 river runoff fields for 30-year periods representing the present-day (yrs. 1976-2005)
195 and future (yrs. 2070-2099; RCP 8.5) periods were obtained from the NOAA GFDL
196 CMIP5 repository.
- 197 2) The differences of the mean seasonal cycles between two periods were computed
198 to form the seasonally varying deltas as monthly averages.
- 199 3) The monthly deltas were bilinearly interpolated both in space and time, and added
200 to the SODA version 2.1.6 (pentad in time and 0.5° latitude x 0.5° longitude¹ with

¹ Although the SODA experiment employs a horizontal resolution of about 0.25° latitude x 0.4° longitude with 40 vertical levels, the final product was released in 0.5° latitude x 0.5° longitude horizontal grid with the same 40 vertical levels.

201 40 vertical levels), CORE version 2 (6 hourly in time and about 1.89° in latitude
202 and longitude), and Dai et al.'s (2009) global river flow (monthly in time and 1° in
203 latitude and longitude) historical data to form a bias-corrected future projection.

204 4) Then, the bias-corrected future atmospheric, oceanic, and river runoff fields were
205 interpolated to the ROMS grid by using the Pyroms package to provide the
206 boundary and initial conditions for the NWA.

207 Selected maps of the GFDL-ESM2M oceanic changes (deltas) are already shown
208 in Fig. 4 and Fig. 5 and discussed in section 2b. The maps of deltas for surface atmospheric
209 forcings and river runoff over the N. Atlantic during December-January-February (DJF)
210 and June-July-August (JJA) are shown in Fig. 6. The changes in surface atmospheric
211 forcings, by design, represent the projected future climate responses to increasing
212 greenhouse gases. For example, surface air temperature over the entire subtropical N.
213 Atlantic warms about 2-3 °C (Fig. 6a). The greenhouse effects contribute to the subtropical
214 warming via increasing surface specific humidity (water vapor; Fig. 6b) and downwelling
215 long-wave radiation (Fig. 6d). The seasonal dependence of specific humidity and long-
216 wave radiative flux are also evident and responsible for the enhanced warming during
217 summer (Fig. 6a). Positive sea level pressure deltas at midlatitudes along with weak or
218 negative sea level pressure deltas in subtropics reduce the surface westerly winds (Fig. 6e).
219 The decreased subtropical precipitation (Fig. 6f) and fresh water flux through rivers (river
220 runoff; Fig. 6g) along with the general increase of precipitation and river runoff at mid-to-
221 high latitudes are consistent with the projected expansion of tropical-subtropical dry zone
222 (Lu et al. 2007; Feng and Fu 2013).

223 Seasonal differences in the deltas, defined as half of the difference between the
224 maximum and minimum monthly values, are shown in Fig. 7 for surface air temperature,
225 surface specific humidity and sea level pressure. The observed interannual variations of
226 annual means during 1976-2005 are also shown in Fig 7 for comparison. The seasonal
227 cycle amplitudes of the deltas are comparable to or larger than the interannual variations
228 along the continental margins of the NWA, underlying the importance of using seasonally
229 varying forcing.

230 *d. Downscaling simulations*

231 We performed a 48-year CTRL (yrs. 1958–2005) and RCP85 (equivalent to yrs.
232 2052-2099) NWA ROMS simulations, and used the last 30 years of each for analyses,
233 allowing for an 18-year spin-up period. We first assessed the downscaled responses,
234 obtained from the difference between the RCP85 and CTRL, over the whole NWA domain,
235 and then present a more detailed analyses of the projections in the Gulf of Maine.

236

237 **3. Downscaled responses over the NWA domain**

238 The downscaled RCP85 responses of SST and surface currents are shown with
239 those of the GFDL ESM2M in Fig. 8. For the ease of comparison, the GFDL-ESM2M
240 responses were bilinearly interpolated to the ROMS grid. One consequence of using a high-
241 resolution ocean model is the redistribution of heat, salt, and momentum. In the wind-
242 driven ocean circulation where vorticity input (wind stress) balances vorticity dissipation
243 (lateral diffusion assuming Munk boundary layer; Munk 1950), the thickness of western

244 boundary layer ε_M is given as $\pi(A_h/\beta)^{1/3}$, where A_H is the horizontal eddy viscosity and
 245 $\beta (= \partial_y f)$ is the variation of Coriolis parameter (f) with latitude. Since ROMS uses 16
 246 times smaller eddy viscosity ($25 \text{ m}^2 \text{ s}^{-1}$) than that of the GFDL-ESM2M ocean model (400
 247 $\text{m}^2 \text{ s}^{-1}$), the western boundary layer thickness reduces to ~ 40 km from ~ 100 km. Therefore,
 248 the Gulf Stream is confined to a narrow western boundary layer as shown in Fig. 8. As a
 249 consequence, SST changes become more pronounced around the U.S. east coast in our
 250 downscaled runs compared to the coarse GFDL-ESM2M. Moreover, the strength of Gulf
 251 Stream is further reduced in the downscaled runs.

252 The position shift of Gulf Stream under the RCP 8.5 scenario has been assessed in
 253 the recent study of Saba et al. (2016), who found that a weakened AMOC in the future
 254 leads to a northward shift of the Gulf Stream's separation from the coast. To determine the
 255 position change of Gulf Stream in our downscaled runs, we compare the horizontal gradient
 256 of sea surface height (SSH) in the RCP85 and CTRL in Fig. 9. Many previous studies used
 257 the SSH gradient to diagnose the position of Gulf Stream (e.g. Andres 2016), since the Gulf
 258 Stream is better represented as the ocean transport (in unit of Sv) rather than the Ekman
 259 dominated surface current. The ocean is approximately in geostrophic balance at low
 260 frequencies, and the SSH gradient is related to the geostrophic velocity as
 261 $f\mathbf{k} \times \mathbf{u}_g = -g\nabla\eta$ (where g is the acceleration due to gravity and \mathbf{u}_g is the geostrophic
 262 velocity). Thus, the SSH gradient represents the changes in ocean transport.

263 In contrast to Saba et al. (2016), our downscaled simulations suggest that the Gulf
 264 Stream separation shifts southward under the RCP 8.5 scenario. Other studies also

265 highlight the lack of consensus on the direction of this shift in response to a change in
266 AMOC; some modeling studies found a northward shift of the Gulf Stream separation in
267 response to a reduction in AMOC, (e.g. Zhang, 2008; Yeager 2015; Saba et al. 2016), while
268 others (e.g. De Coëtlogon et al. 2006; Kwon and Frankignoul 2014) found a southward
269 shift, as in our downscaling simulations.

270 The warming of bottom temperatures around the U.S. East Coast is enhanced in the
271 downscaled run compared to the coarse resolution GFDL-ESM2M (Fig. 10). The enhanced
272 warming is pronounced along the continental shelf and shelf break along the Gulf of
273 Mexico and the U.S. East Coast, indicating about a 4°C warming, 1-2°C more than that
274 projected in the coarse resolution GFDL-ESM2M. Enhanced warming of about 1°C over
275 the Gulf of Maine and the Gulf of Saint Lawrence is also evident.

276 In addition to inducing long-term hydrographic changes under the RCP 8.5
277 scenario, the increased radiative forcings also impact the occurrence of ocean eddies. The
278 SSH variance ($\overline{\eta'^2}$), a measure of eddy activity, is shown in Fig. 11 for the CTRL and the
279 RCP85 simulations during DJF and JJA. Here we decomposed the 5-day mean (pentad)
280 SSH data as the sum of low-pass filtered component and anomaly to this low-passed
281 component as $\eta = \bar{\eta} + \eta'$. The 24-pentad (equivalent to 120-day) running mean, based
282 upon the typical eddy characteristic period over the model domain [50 – 100 days in the
283 Caribbean (Jouanno et al. 2008) and about 90 days for the long-lived eddies in Gulf Stream
284 (Kang and Curchister 2013)] forms the low pass filter.

285 The CTRL simulation captures the observed seasonal cycle of eddy occurrence in
286 the North Atlantic as well as in the Gulf of Mexico (Fig. 11b). Over the Gulf Stream region,
287 eddy activity dominates during summer, though the spatial pattern of eddy activity is
288 similar in summer and winter (e.g. Zhai et al. 2008). As in observations (e.g. Chang and
289 Oey 2012), the Loop Current appears to shed more eddies during summer than in winter in
290 the Gulf of Mexico.

291 The changes of eddies in response to increasing radiative forcing are also larger
292 during summertime, though the main response of the Gulf Stream and Loop Current eddies
293 are very different. While eddy activity along the Gulf Stream indicates a southward shift
294 under the RCP 8.5 scenario consistent with the shift in Gulf Stream separation, Loop
295 Current eddies in the Gulf of Mexico show an increased occurrence under the RCP 8.5
296 scenario.

297

298 **4. Coastal environment projections: Gulf of Maine**

299 Here we examine the climatic changes within the Gulf of Maine in greater detail,
300 given the strong warming that has already occurred there and is projected to continue into
301 the future (e.g. Saba et al. 2016; see our Figs. 8 and 10). An accurate representation of the
302 present-day coastal circulation is likely to be critical to obtain the three dimensional
303 structures of changes in the future. As shown in Fig. 12 (see also the schematics in Fig. 2),
304 our downscaled simulations capture the essence of the Gulf of Maine circulation, including
305 the topographically trapped Gulf of Maine Coastal Plume (GMCP; Keafer et al. 2005) and

306 Maine Coastal Current (MCC; [Anderson et al. 2014](#)). It is also clear that the summertime
307 cyclonic MCC forms in combination with Atlantic water that enters the Gulf through the
308 Northeast Channel and exits through the Great South and Northeast channels. The
309 summertime cyclonic MCC is further strengthened in response to RCP8.5 forcings ([Fig.](#)
310 [12](#)). The warming is amplified along the sill depth of the Northeast Channel, suggesting
311 that a substantial fraction of the warming can be traced to the open ocean.

312 The open ocean influence on the Gulf of Maine is examined further using a cross
313 section at 42°N latitude ([Fig. 13](#)), the same cross section as used in [Saba et al. \(2016\)](#). The
314 zonal and vertical velocity changes are shown as vectors, the anomalous northward
315 meridional velocities are dotted, the temperature changes are color shaded, and the salinity
316 differences are contoured. [Figure 13](#) clearly shows the enhanced intrusion of warm and
317 saline open ocean waters into the Gulf through the channel, resulting in warm saline waters
318 at depth in the Gulf. The strengthening of the present-day thermohaline front is also
319 noticeable and may be responsible for the enhanced intrusion of slope waters. These results
320 are qualitatively consistent with the study of [Saba et al. \(2016\)](#), though the magnitudes of
321 changes are much smaller than their estimates.

322 It is also noteworthy that the sources of those warm and salty slope waters may
323 differ between this study and [Saba et al. \(2016\)](#). Observations indicate that the Gulf of
324 Maine waters at depth are composed of a mixture of surface and deep waters flowing into
325 the Gulf: they are Scotian Shelf Water from the Nova Scotian shelf that enters the Gulf at
326 the surface and slope waters that enter at depth through the Northeast Channel (e.g.
327 [Townsend et al. 2014](#)). There are two distinct types of slope waters: one is Labrador Slope

328 Water and the other is Atlantic Temperate Slope Water (e.g. Bigelow 1927; Ramp et al.
329 1985; Smith et al. 2001; Townsend et al. 2014; Townsend et al. 2015).

330 To highlight the source water masses that impact the Gulf of Maine in the CTRL
331 and RCP85 simulations, we estimated the backward trajectory of particles by using
332 TRACMASS (Döös 1995; Döös et al. 2017; <http://tracmass.org>) on the output of the
333 currents from both ROMS simulations. We initialized 1,521 particles at 5-day intervals
334 from June 2nd to August 31st (a total of 28,899 particles) over the region (41.63-44.61°N;
335 69.90-65.96°W; thick black box in Fig. 14) between the depths of 145 and 327 m. These
336 particles were tracked backward by using the mean annual cycle of three-dimensional
337 velocities at a daily time resolution. While the zonal and meridional velocities were
338 obtained from the CTRL and RCP85 runs, the mean annual cycle of vertical velocity was
339 estimated using the continuity equation. Then, the TRACMASS model was integrated
340 backward for 1,000 days starting from August 31st.

341 The water masses that contribute to Gulf of Maine bottom waters in the current
342 climate settings are illustrated in Fig. 14 by randomly choosing 20 particle trajectories. It
343 largely conforms to previous studies on the composition of Gulf of Maine bottom waters,
344 which consist of a mixture of Atlantic Temperate Slope Waters (Gulf Stream), Labrador
345 Subarctic Slope Waters, and Scotian Shelf Waters. There is also substantial recirculation
346 of Gulf Stream waters before they enter the Gulf of Maine.

347 The maps of instantaneous particle density in CTRL and RCP85 runs at 200, 500,
348 and 1,000 days before the initial time (August 31st) are shown in Fig. 15 (see movie clip,
349 Fig. S2 of Supplementary Information, for time varying maps of particle density). We

350 estimated the particle density by counting the number of particles over the whole water
351 column within $1^\circ \times 1^\circ$ grid boxes. At the first 200-day backward tracking, the Gulf of Maine
352 bottom waters are mostly influenced by the Scotian Shelf Waters. Further back in time
353 (500 and 1,000 days before the initial time), the Labrador Subarctic Slope Waters and, to
354 a lesser extent, Atlantic Temperate Slope Waters impact the composition of Gulf of Maine
355 bottom waters.

356 The percentage change of particle densities over time (instantaneous number of
357 particles divided by initial number of particles) over the Gulf of Maine, subtropical N.
358 Atlantic ($\leq 36^\circ\text{N}$), and subpolar N. Atlantic ($> 36^\circ\text{N}$) are shown in [Fig. 16](#). During the
359 1,000-day backward integration of TRACMASS, contributions from the subtropical N.
360 Atlantic (i.e. Atlantic Temperate Slope Waters) are negligible compared to the subpolar N.
361 Atlantic (i.e. Labrador Subarctic Slope Waters). There is substantial recirculation of Gulf
362 Stream Waters before entering into the Gulf of Maine (see [Fig. 14](#)), and thus the Atlantic
363 Temperate Slope Waters may lose their characteristics by intense mixing before impacting
364 the Gulf of Maine bottom waters.

365 [Figures 15 and 16](#) indicate that the source waters for the Gulf Maine are very similar
366 in the CTRL and RCP8.5, including the absence of Gulf Stream waters in the latter. Then
367 why does the Gulf of Maine warm so intensively in the future? The answer may lie in
368 where the temperatures change the most over the N. Atlantic, rather than on where the
369 water originated from. In this regard, the intense warming southeast of Newfoundland in
370 response to increased radiative forcing appears in most coupled climate model simulations
371 (e.g. [Alexander et al. 2019](#)), including the GFDL-ESM2M. Indeed, the change in

372 temperature between 2070-2099 and 1976-2005 exceeds 5°C at the surface and 8°C at 200
373 m depth in the vicinity of 46°N, 45°W in GFDL-ESM2M RCP 8.5 simulation ([Alexander](#)
374 [et al. 2019](#)). The backward particle trajectory results suggest that this very warm water is
375 transported to the Gulf of Maine, and thus the Gulf of Maine warming is predominately
376 forced by changes in the source water properties rather than changes in source water
377 contributions.

378

379 **5. Summary and concluding remarks**

380 In this study, we downscaled the GFDL-ESM2M projected ocean climate changes
381 along the U.S. East and Gulf coasts using ROMS, an eddy-resolving regional ocean model.
382 The large-scale climate change forcings were obtained from the mean difference (i.e.
383 deltas) between the period yrs. 2070-2099 and yrs. 1976-2005. We extended previous
384 versions of this method (e.g. [Auad et al. 2006](#); [Liu et al. 2012](#); [van Hooidek et al. 2015](#))
385 by including a seasonal cycle of the deltas to address the strong seasonal dependence of
386 climate change (e.g., [Partanen et al. 2017](#)). While the delta method removes the mean
387 (present-day) bias and enhances the signal-to-noise ratio of the response, it neglects
388 changes in interannual climate variability. Therefore, our approach can be viewed as a
389 sensitivity test of the response of the coastal ocean to future changes in radiation.

390 The downscaled climate projection indicates enhanced warming of ocean bottom
391 temperatures relative to the global climate model around the U.S. East and Gulf coasts,
392 particularly along the continental shelf and shelf break. Enhanced warming also occurs in

393 the Gulf of Maine and Gulf of Saint Lawrence. We attribute the enhanced warming to the
394 improved simulations of coastal ocean hydrography in ROMS. The ROMS control
395 simulation resolved the essence of observed coastal ocean circulation. For example, ROMS
396 captures the topographically trapped GMCP and MCC in the Gulf of Maine and intrusion
397 of open ocean waters through the Northeast Channel. In response to increasing radiative
398 forcing, the intrusion of slope waters is increased and summertime cyclonic MCC is further
399 strengthened. This leads to enhanced warming in the Gulf of Maine preferentially at depth
400 following the sill depth of Northeast Channel, consistent with [Saba et al. \(2016\)](#).

401 However, in contrast to [Saba et al. \(2016\)](#), we find that the role of Atlantic
402 Temperate Slope Waters (Gulf Stream Waters) on projected warming at depth in the Gulf
403 of Maine is relatively minor compared to the contribution of Labrador Subarctic Slope
404 Waters. Backward trajectories of particles indicate that Gulf of Maine waters can originate
405 primarily from the subpolar N. Atlantic rather than the subtropics. Given the dramatic
406 warming off the coast of Newfoundland and Labrador in climate projections, our results
407 suggest this advective pathway as a key driver for the projected Gulf of Maine warming.
408 Thus, monitoring and modeling of the subpolar N. Atlantic are crucial to improve our
409 understanding of changes in the Gulf of Maine.

410 In closing, some previous studies (e.g. [Brooks 1987](#)) suggested the important role
411 of eddies in hydrographic changes over the Gulf of Maine. For example, occasional
412 propagations of Gulf Stream warm core rings into the regions impact Gulf of Maine
413 temperatures at depth by modifying the characteristics of slope waters. Our downscaled
414 projection shows substantial changes in eddies in response to RCP 8.5 radiative forcings.

415 However, the detailed dynamical linkage between the Gulf Stream eddies and the
416 hydrographic changes over the Gulf of Maine, and the relative importance of the eddy
417 impacts on the mean circulation changes remains to be assessed in future studies.

418

419 *Acknowledgment.* This work was supported by NOAA/CPO COCA program, grant #NA-
420 15OAR4310133. We thank Drs. Charles Stock and Enrique Curchitser for discussion on
421 the results. We also thank Dr. Michael Jacox for his insightful comments on the manuscript.

422

423 **FIGURE CAPTIONS**

424 **Fig. 1.** (left) Wintertime (DJF) temperature (shading) and currents (arrows) at 5 m depth
425 over the Gulf of Maine during the yrs. 1976-2005 derived from (top) the coarse
426 resolution GFDL ESM2M and (bottom) the fine resolution ROMS. (right) The
427 same as the left but for the patterns at depth (155 m).

428 **Fig. 2.** a) Schematics of major current systems in our downscaling domain covers the
429 Northwest Atlantic Ocean and Gulf of Mexico (NWA). Thick gray dashed line
430 indicates the position of open boundaries of NWA. b) Major current systems in
431 Gulf of Maine (denoted as gray shading in a) shown with solid arrows: black -
432 Maine Coastal Current (MCC); grey - Gulf of Maine Coastal Plume (GMCP).
433 Abbreviations used: MA – Massachusetts; NH – New Hampshire; ME – Maine.

434 **Fig. 3.** Maps of annually averaged surface current derived from (left) satellite-tracked
435 surface buoy dataset (averaged over during January 1979 - March 2015; [Lumpkin
436 and Johnson 2013](#)), (middle) ROMS CTRL (averaged over during yrs. 1976-
437 2005), and (right) SODA version 2.1.6 dataset (averaged over during yrs. 1976-
438 2005). The colors indicate the speed of surface current.

439 **Fig. 4.** (top) Maps of DJF GFDL-ESM2M responses of ocean surface (left) temperature,
440 (middle) salinity, and (right) current to RCP 8.5 radiative forcing changes,
441 estimated as the mean differences between two time periods representing future
442 (yrs. 2070-2099) and present-day (yrs. 1976-2007) climate conditions. (bottom)
443 The same as the top but for the JJA.

444 **Fig. 5.** (top) Maps of DJF GFDL-ESM2M responses of ocean bottom temperature to RCP
445 8.5 radiative forcing changes, estimated as the mean differences between two time
446 periods representing future (yrs. 2070-2099) and present-day (yrs. 1976-2007)
447 climate conditions. (bottom) The same as the top but for the JJA.

448 **Fig. 6.** Maps of DJF and JJA GFDL-ESM2M responses of a) surface air temperature, b)
449 surface specific humidity, c) downwelling solar short wave radiation, d)
450 downwelling long wave radiation, e) sea level pressure and surface (10 m) winds,
451 f) rainfall rate, and g) river runoff to RCP 8.5 radiative forcing changes, estimated
452 as the mean differences between two time periods representing future (yrs. 2070-
453 2099) and present-day (yrs. 1976-2007) climate conditions.

454 **Fig. 7.** (top) Maps of the amplitude of seasonal cycle of delta for a) surface air
455 temperature, b) surface specific humidity, and c) sea level pressure, where the
456 amplitude is defined as a half of the difference between the maximum and
457 minimum of monthly delta. (bottom) The standard deviation of annual means of
458 corresponding fields during yrs. 1976-2005 derived from CORE version 2 data set
459 ([Large and Yeager 2009](#)).

460 **Fig. 8.** (top) Maps of projected DJF sea surface temperature (color shadings) and surface
461 current (vectors) responses, derived from a) ROMS downscaling and b) GFDL
462 ESM2M simulations. For the ease of comparisons, the GFDL ESM2M responses
463 were bilinearly interpolated to the ROMS grid, and the differences, a) minus b),
464 are shown in c). (bottom) The same as the top but for the JJA.

465 **Fig. 9.** Horizontal gradient maps of annually averaged sea surface height derived from a)
 466 RCP85 and b) CTRL simulations. The differences, a) minus b), are shown in c).

467 **Fig. 10.** (top) Maps of projected DJF ocean bottom temperature responses, derived from a)
 468 ROMS downscaling and b) GFDL ESM2M simulations. For the ease of
 469 comparisons, the GFDL ESM2M responses were bilinearly interpolated to the
 470 ROMS grid, and the differences, a) minus b), are shown in c). The grey contours
 471 in each map represent 200 m isobath. (bottom) The same as the top but for the JJA.

472 **Fig. 11.** (top) Maps of DJF high pass filtered transient ocean eddy statistics derived as sea
 473 surface height variance, $\overline{\eta'^2}^{1/2}$, in a) RCP85 and b) CTRL simulations. The
 474 differences, a) minus b), are shown in c). See text for the details of ocean eddy
 475 statistics estimation. (bottom) The same as the top but for the JJA.

476 **Fig. 12.** (top) Maps of projected a) DJF and b) JJA temperature (color shadings) and current
 477 (vectors) responses at surface derived from ROMS downscaling exercise. (bottom)
 478 The same as the top but for the responses at ocean bottom. The thick black line A
 479 in the bottom panel represents the zonal cross section (42°N latitude) used in Fig.
 480 13.

481 **Fig. 13.** Zonal cross section of projected a) DJF and b) JJA temperature (color shadings),
 482 salinity (white contours), and zonal and vertical current (vectors) responses
 483 derived from ROMS downscaling runs along the line A (see Fig. 12). The
 484 anomalous northward meridional velocities are striped. Negative (zero) salinity
 485 changes are denoted as dashed (thick) white contours.

486 **Fig. 14.** The initial location map of 28,899 particles. The location is denoted as thick black
487 box representing the volumes spanning 41.63-44.61°N, 69.90-65.96°W, and 145-
488 327 m. The colored lines denote the three-dimensional backward tracking of
489 randomly chosen 20 particles located initially within the box for 1,000 days. The
490 grey shaddings in each map represent the continental shelves where the water
491 depth is shallower than 200 m.

492 **Fig. 15.** (top) Maps of particle density at a) 200, b) 500, and c) 1,000 days before the initial
493 time (June 2nd) derived from RCP85 run. (bottom) The same as the top but for the
494 CTRL. See text for the details of backward particle tracking and particle density
495 estimation. The grey contours in each map represent 200 m isobath.

496 **Fig. 16.** a) Percentage changes of particle densities over time, integrated over the Gulf of
497 Maine (black line), subtropical N. Atlantic (red line), and subpolar N. Atlantic
498 (blue line), derived from the RCP85 run. b) The same as a) but for the CTRL.

499

500

501 **REFERENCES**

- 502 Alexander, M., S.-I. Shin, J. D. Scott, E. Curchitser, and C. Stock, 2019: The response of
503 the northwest Atlantic Ocean to climate change. *J. Climate*, submitted. (available
504 at <https://www.esrl.noaa.gov/psd/people/michael.alexander/publications.html>).
- 505 Anderson, D. L., and Coauthors, 2004: The new GFDL global atmosphere and land model
506 AM2-LM2: Evaluation with prescribed SST simulations. *J. Climate*, **17**, 4641–
507 4673.
- 508 Anderson, D. M., and Coauthors, 2014: Understanding interannual, decadal level
509 variability in paralytic shellfish poisoning toxicity in the Gulf of Maine: The HAB
510 index. *Deep-Sea Res. II*, **103**, 264-276.
- 511 Andres, M., 2016: On the recent destabilization of the Gulf Stream path downstream of
512 Cape Hatteras. *Geophys. Res. Lett.*, **43**, doi:10.1002/2016GL069966.
- 513 Auad, G, A. Miller, and E. Di Lorenzo, 2006: Long-term forecast of oceanic conditions off
514 California and their biological implications. *J. Geophys. Res.*, **111**, C09008,
515 doi:10.1029/2005JC003219.
- 516 Bigelow, H. B., 1927: Physical oceanography of the Gulf of Maine. *Bull. U.S. Bur. Fish.*,
517 **40**, 511–1027.
- 518 Brooks, D. A., 1987: The influence of warm-core rings on the slope water entering the Gulf
519 of Maine. *J. Geophys. Res.*, **92**, 8183-8196.

- 520 Buckley, M. and J. Marshall, 2016: Observations, inferences, and mechanisms of the
521 Atlantic Meridional Overturning Circulation: A review. *Rev. Geophys.*, **54**, 5–63.
- 522 Caesar, L., S. Rahmstorf, A. Robinson, G. Feulner, and V. Saba, 2018: Observed
523 fingerprint of a weakening Atlantic Ocean overturning circulation. *Nature*, **256**,
524 191-196.
- 525 Carton, J. A., and B. S. Giese, 2008: A reanalysis of ocean climate using Simple Ocean
526 Data Assimilation (SODA). *Mon. Wea. Rev.*, **136**, 2999–3017.
- 527 Chang, Y.-L., and L.-Y. Oey, 2012: Why does the Loop Current tend to shed more eddies
528 in summer and winter? *Geophys. Res. Lett.*, **39**, L05605,
529 doi:10.1029/2011GL050773.
- 530 Cheng, W., J. C. H. Chiang, and D. Zhang, 2013: Atlantic Meridional Overturning
531 Circulation (AMOC) in CMIP5 models: RCP and historical simulations. *J. Climate*,
532 **26**, 7187–7197.
- 533 Curchitser, E. N., D. B. Haidvogel, A. J. Hermann, E. Dobbins, T. M. Powell, and A.
534 Kaplan, 2005: Multi-scale modeling of the North Pacific Ocean: Assessment of
535 simulated basin-scale Variability (1996-2003). *J. Gophys. Res.*, **110**, C11021,
536 doi:101029/2005JC002902.
- 537 Dai, A., T. Qian, K. E. Trenberth, and J. D. Milliman, 2009: Changes in continental
538 freshwater discharge from 1948–2004. *J. Climate*, **22**, 2773– 2792.

- 539 De Coëtlogon, G., C. Frankignoul, M. Bentsen, C. Delon, H. Haak, S. Masina, and A.
540 Pardaens, 2006: Gulf Stream variability in five ocean general circulation models.
541 *J. Phys. Oceanogr.*, **36**, 2119-2135.
- 542 Döös, K., 1995: Inter-ocean exchange of water masses. *J. Geophys. Res.*, **100**, 13499–
543 13514.
- 544 Döös, K., B. Jönsson, and J. Kjellsson, 2017: Evaluation of oceanic and atmospheric
545 trajectory schemes in the TRACMASS trajectory model v6.0. *Geosci. Model Dev.*,
546 **10**, 1733–1749.
- 547 Dunne, J. P., and Coauthors, 2012: GFDL’s ESM2 Global Coupled Climate–Carbon Earth
548 System Models. Part I: Physical Formulation and Baseline Simulation
549 Characteristics. *J. Climate*, **25**, 6646-6665.
- 550 Feng, S., and Q. Fu, 2013: Expansion of global drylands under a warming climate. *Atmos.*
551 *Chem. Phys.*, **13**, 10081-10094.
- 552 Griffies, S. M., and Coauthors, 2005: Formulation of an ocean model for global climate
553 simulations. *Ocean Sci.*, **1**, 45–79.
- 554 Griffies, S. M., and Coauthors, 2015: Impacts on ocean heat from transient mesoscale
555 eddies in a hierarchy of climate models. *J. Climate*, **28**, 952–977.
- 556 He, J., and B. J. Soden, 2016: The impact of SST biases on projections of anthropogenic
557 climate change: A greater role for atmosphere-only models? *Geophys. Res. Lett.*,
558 **43**, 7745-7750.

- 559 Hoegh-Guldberg, O., and J. F. Bruno, 2010: The impact of climate change on the world's
560 marine ecosystems. *Science*, **328**, 1523-1528.
- 561 IPCC, 2013: Climate Change 2013: The Physical Science Basis. Contribution of Working
562 Group I to the Fifth Assessment Report of the Intergovernmental Panel on Climate
563 Change [Stocker, T. F., D. Qin, G.-K. Plattner, M. Tignor, S. K. Allen, J. Boschung,
564 A. Nauels, Y. Xia, V. Bex and P. M. Midgley (eds.)]. Cambridge University Press,
565 Cambridge, United Kingdom and New York, NY, USA, 1535 pp.
- 566 Kang, D., and E. N. Curchister, 2013: Gulf Stream eddy characteristics in a high-resolution
567 ocean model. *J. Geophys. Res.*, **118**, 4474-4487.
- 568 Kang, D., and E. N. Curchitser, 2015: Energetics of eddy-mean flow interactions in the
569 Gulf Stream region. *J. Phys. Oceanogr.*, **45**, 1103-1120.
- 570 Keafer, B. A., J. H. Churchill, D. J. McGillicuddy Jr., D. M. Anderson, 2005: Bloom
571 development and transport of toxic *Alexandrium fundyense* populations within a
572 coastal plume in the Gulf of Maine. *Deep-Sea Res. II*, **52**, 2674–2697.
- 573 Kwon, Y.-O., and C. Frankignoul, 2014: Mechanisms of multidecadal Atlantic meridional
574 overturning circulation variability diagnosed in depth versus density space. *J.*
575 *Climate*, **27**, 9359-9376.
- 576 Jouanno, J., J. Sheinbaum, B. Barnier, J.-M. Molines, L. Debreu, and F. Lemarié, 2008:
577 The mesoscale variability in the Caribbean Sea. Part I: Simulations and
578 characteristics with an embedded model. *Ocean Model.*, **23**, 82–101.

- 579 Large, W. G., and S. G. Yeager, 2009: The global climatology of an interannually varying
580 air-sea flux data set. *Clim. Dyn.*, **33**, 341–364.
- 581 Le Bris, A., and Coauthors, 2017: Climate vulnerability and resilience in the most valuable
582 North American fishery. *PNAS*, **115**, 1831-1836.
- 583 Liu, Y., S.-K. Lee, B. A. Muhling, J. T. Lamkin and D.B. Enfield, 2012: Significant
584 reduction of the Loop Current in the 21st century and its impact on the Gulf of
585 Mexico. *J. Geophys. Res.*, **117**, C05039.
- 586 Lu, J., G. A. Vecchi, and T. Reichler, 2007: Expansion of the Hadley cell under global
587 warming. *Geophys. Res. Lett.*, **34**, L06805, doi:10.1029/ 2006GL028443.
- 588 Lumpkin, R., and G. C. Johnson, 2013: Global ocean surface velocities from drifters:
589 Mean, variance, El Nino–Southern Oscillation response, and seasonal cycle. *J.*
590 *Geophys. Res. Oceans*, **118**, 2992–3006.
- 591 Munk, W. H., 1950: On the wind-driven ocean circulation. *J. Meteor.*, **7**, 79-93.
- 592 Partanen, A.-I., M. Leduc, and H. D. Matthews, 2017: Seasonal climate change patterns
593 due to cumulative CO₂ emissions. *Environ. Res. Lett.*, **12**, 075002.
- 594 Pershing, A. J., and Coauthors, 2015: Slow adaptation in the face of rapid warming leads
595 to collapse of the Gulf of Maine cod fishery. *Science*, **350**, 809-812.
- 596 Ramp, S. R., R. J. Schlitz, and W. R. Wright, 1985: The deep flows through the Northeast
597 Channel, Gulf of Maine. *J. Phys. Oceanogr.*, **15**, 1790–1808.

- 598 Saba, V. S., and Coauthors, 2016: Enhanced warming of the Northwest Atlantic Ocean
599 under climate change. *J. Geophys. Res. Oceans*, **121**, 118–132.
- 600 Shchepetkin, A. F., and J. C. McWilliams, 2005: The Regional Oceanic Modeling System
601 (ROMS): A split-explicit, free-surface, topography- following-coordinate oceanic
602 model. *Ocean Modell.*, **9**, 347–404.
- 603 Small, R. J., and Coauthors, 2014: A new synoptic scale resolving global climate
604 simulation using the Community Earth System Model. *J. Adv. Model. Earth Syst.*,
605 **6**, 1065–1094.
- 606 Smith P. C., W. W. Houghton, R. G. Fairbanks, and D. G. Mountain, 2001: Interannual
607 variability of boundary fluxes and water mass properties in the Gulf of Maine and
608 on Georges Bank: 1993–1997. *Deep-Sea Res. II*, **48**, 37–70.
- 609 Taylor, K. E., R. J. Stouffer, and G. A. Meehl, 2012: An overview of CMIP5 and the
610 experiment design. *Bull. Amer. Meteor. Soc.*, **93**, 485-498.
- 611 Townsend, D. W., D. J. McGillicuddy Jr., M. A. Thomas, and N. D. Rebeck, 2014:
612 Nutrients and water masses in the Gulf of Maine–Georges Bank region: Variability
613 and importance to blooms of the toxic dinoflagellate *Alexandrium fundyense*. *Deep-*
614 *Sea Res. II*, **103**, 238-263.
- 615 Townsend, D. W., and Coauthors, 2015: Water masses and nutrient sources to the Gulf of
616 Maine. *J. Mar. Res.*, **73**, 93-122.

- 617 van Hooidek, R., J. A. Maynard, Y. Liu, and S.-K. Lee, 2015: Downscaled projections of
618 Caribbean coral bleaching that can inform conservation planning. *Global Change*
619 *Biol.*, **21**, 3389-3401.
- 620 Yeager, S., 2015: Topographic coupling of the Atlantic overturning and gyre circulations.
621 *J. Phys. Oceanogr.*, **45**, 1258-1284.
- 622 Zhai, X., R. J. Greatbatch, and J.-D. Kohlmann, 2008: On the seasonal variability of eddy
623 kinetic energy in the Gulf Stream region. *Geophys. Res. Lett.*, **35**, L24609,
624 doi:10.1029/2008GL036412.
- 625 Zhang, R., 2008: Coherent surface-subsurface fingerprint of the Atlantic meridional
626 overturning circulation. *Geophys. Res. Lett.*, **35**, L20705,
627 doi:10.1029/2008GL035463.
- 628

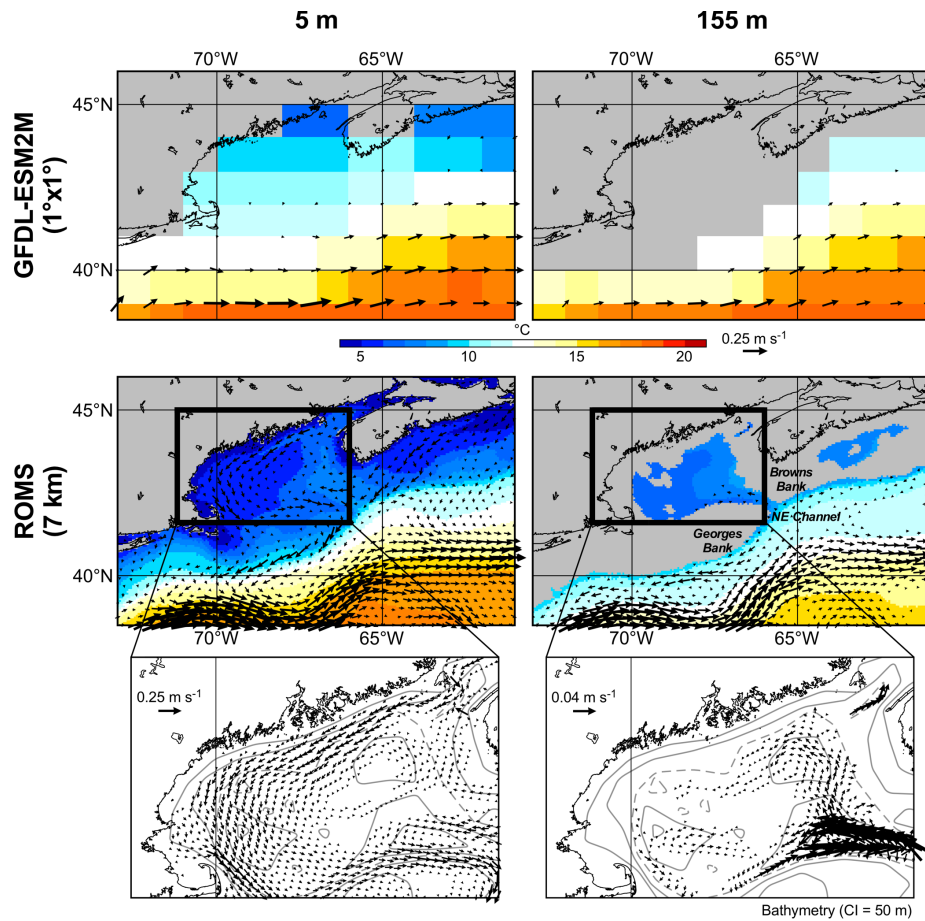
1 **Table 1.** Atmospheric forcing variables used to estimate seasonally varying delta.

ROMS (GFDL-ESM2M)*	Description	Units	Resolution
pair (psl)	Sea Level Pressure	Pa	
qair (huss)	Surface Specific Humidity	kg kg ⁻¹	
tair (tas)	Surface Air Temperature	°C	
uwind (uas)	10 m U-wind Component	m s ⁻¹	T63
vwind (vas)	10 m V-wind Component	m s ⁻¹	(CORE2)
lwrad_down (rlds)	Downwelling LW Radiation	W m ⁻²	
sward (rsds)	Downwelling SW Radiation	W m ⁻²	
rain (pr)	Rainfall Rate	kg (m ⁻² s ⁻¹)	
runoff (friver)	River Runoff	kg (m ⁻² s ⁻¹)	Dai & Trenberth Discharge Grid

2 * Here we followed the nomenclature of ROMS (CMIP5) standard.

3

4



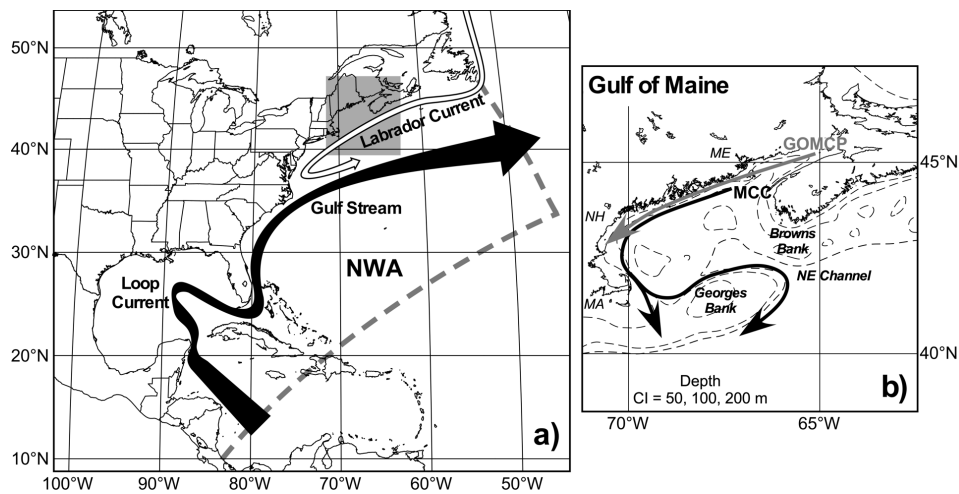
5

6 **Fig. 1.** (left) Wintertime (DJF) temperature (shading) and currents (arrows) at 5 m depth
 7 over the Gulf of Maine during the yrs. 1976-2005 derived from (top) the coarse
 8 resolution GFDL ESM2M and (bottom) the fine resolution ROMS. (right) The
 9 same as the left but for the patterns at depth (155 m).

10

11

12



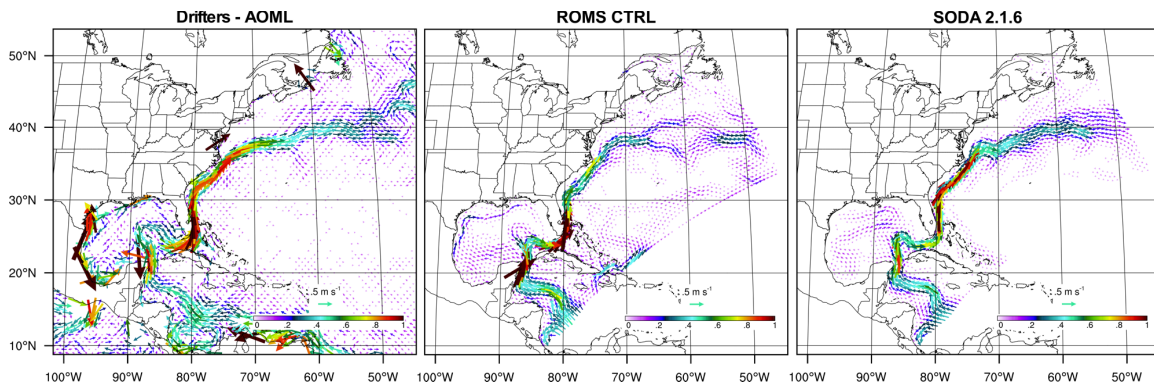
13

14 **Fig. 2.** a) Schematics of major current systems in our downscaling domain covers the
 15 Northwest Atlantic Ocean and Gulf of Mexico (NWA). Thick gray dashed line
 16 indicates the position of open boundaries of NWA. b) Major current systems in
 17 Gulf of Maine (denoted as gray shading in a) shown with solid arrows: black -
 18 Maine Coastal Current (MCC); grey - Gulf of Maine Coastal Plume (GMCP).
 19 Abbreviations used: MA – Massachusetts; NH – New Hampshire; ME – Maine.

20

21

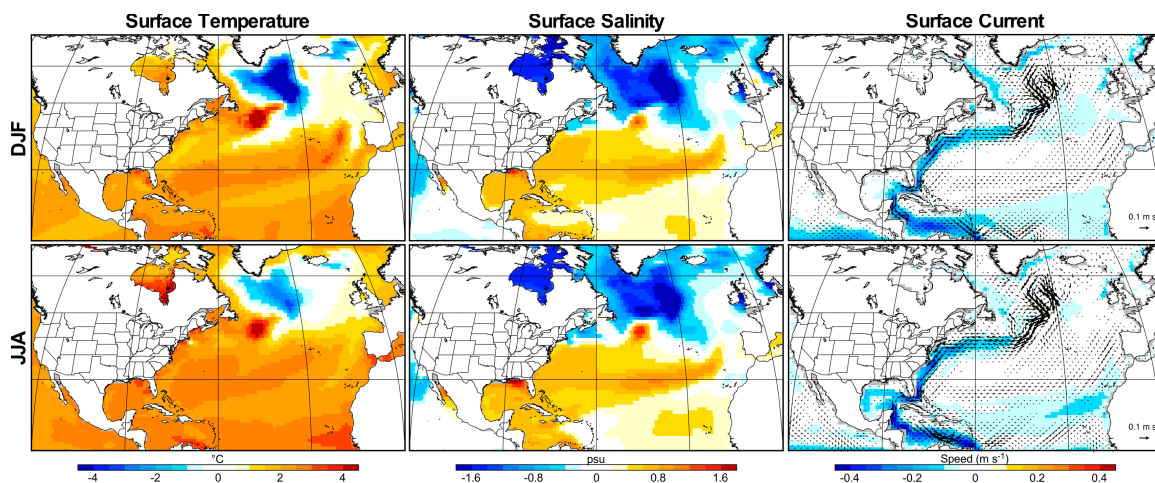
22



23 **Fig. 3.** Maps of annually averaged surface current derived from (left) satellite-tracked
24 surface buoy dataset (averaged over during January 1979 - March 2015;
25 [Lumpkin and Johnson 2013](#)), (middle) ROMS CTRL (averaged over during yrs.
26 1976-2005), and (right) SODA version 2.1.6 dataset (averaged over during yrs.
27 1976-2005). The colors indicate the speed of surface current.

28

29

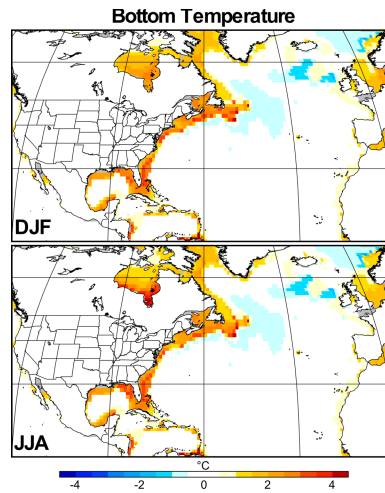


30

31 **Fig. 4.** (top) Maps of DJF GFDL-ESM2M responses of ocean surface (left) temperature,
 32 (middle) salinity, and (right) current to RCP 8.5 radiative forcing changes,
 33 estimated as the mean differences between two time periods representing future
 34 (yrs. 2070-2099) and present-day (yrs. 1976-2007) climate conditions. (bottom)
 35 The same as the top but for the JJA.

36

37

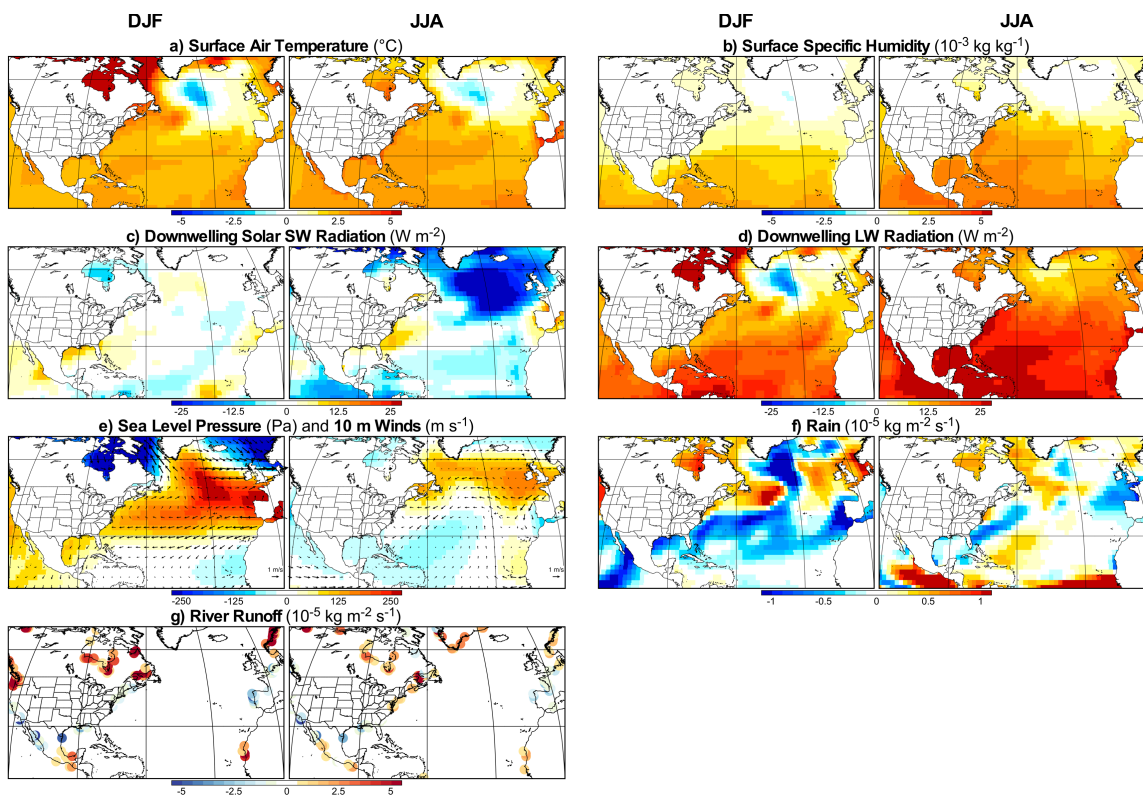


38

39 **Fig. 5.** (top) Maps of DJF GFDL-ESM2M responses of ocean bottom temperature to
40 RCP 8.5 radiative forcing changes, estimated as the mean differences between
41 two time periods representing future (yrs. 2070-2099) and present-day (yrs.
42 1976-2007) climate conditions. (bottom) The same as the top but for the JJA.

43

44

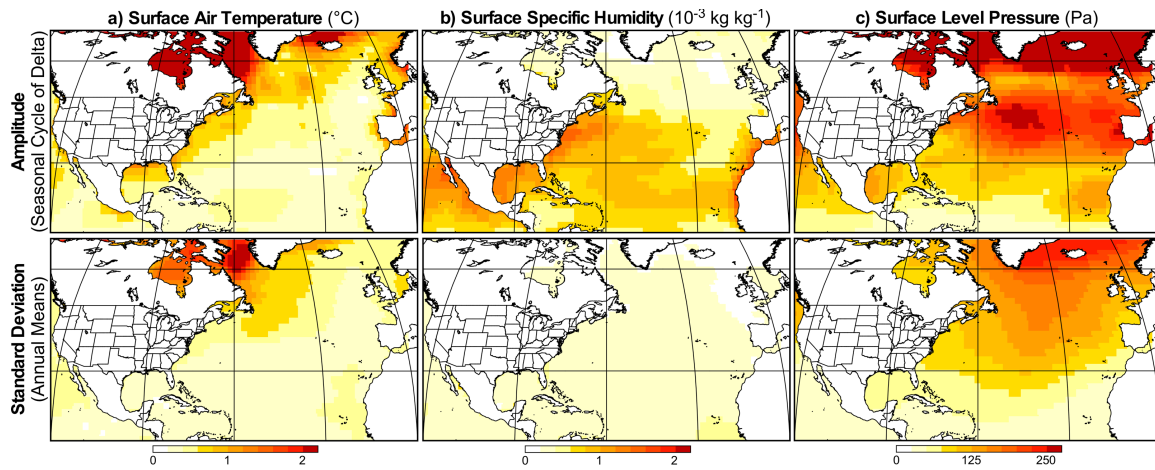


45

46 **Fig. 6.** Maps of DJF and JJA GFDL-ESM2M responses of a) surface air temperature, b)
 47 surface specific humidity, c) downwelling solar short wave radiation, d)
 48 downwelling long wave radiation, e) sea level pressure and surface (10 m) winds,
 49 rainfall rate, and g) river runoff to RCP 8.5 radiative forcing changes,
 50 estimated as the mean differences between two time periods representing future
 51 (yrs. 2070-2099) and present-day (yrs. 1976-2007) climate conditions.

52

53

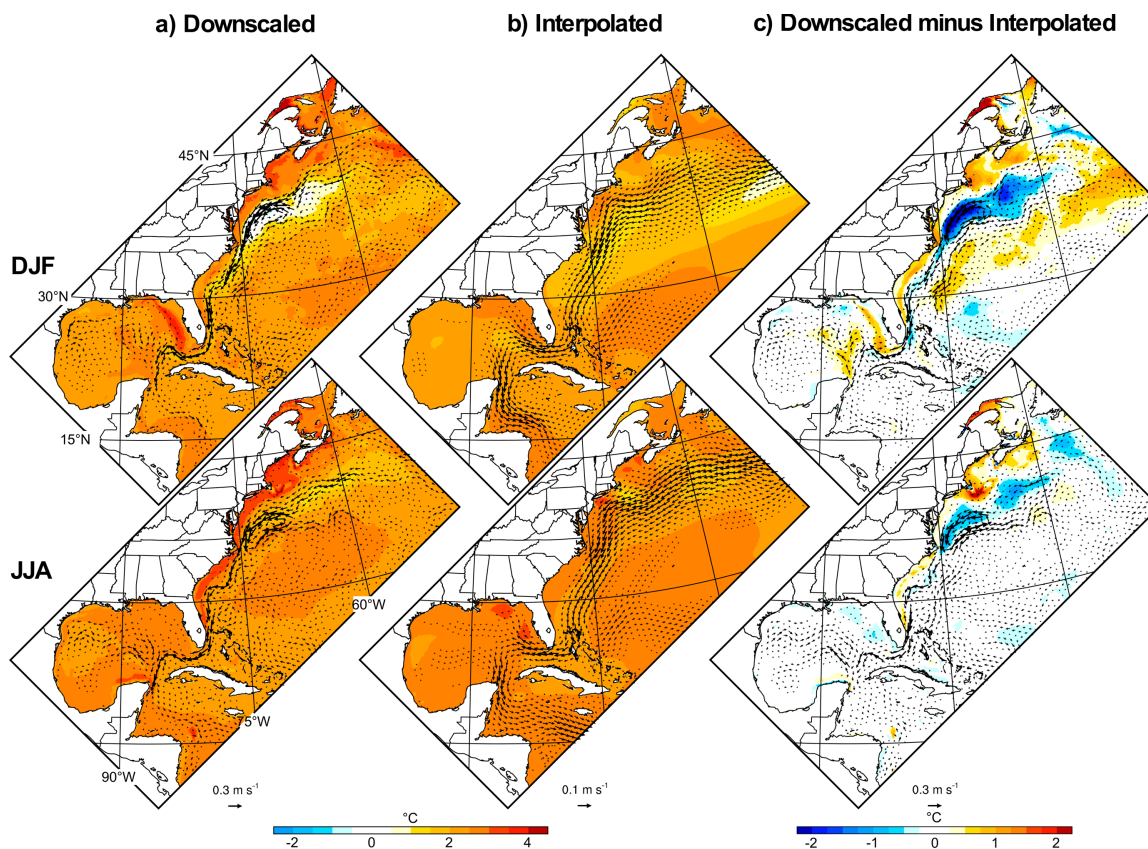


54

55 **Fig. 7.** (top) Maps of the amplitude of seasonal cycle of delta for a) surface air
 56 temperature, b) surface specific humidity, and c) sea level pressure, where the
 57 amplitude is defined as a half of the difference between the maximum and
 58 minimum of monthly delta. (bottom) The standard deviation of annual means of
 59 corresponding fields during yrs. 1976-2005 derived from CORE version 2 data
 60 set (Large and Yeager 2009).

61

62

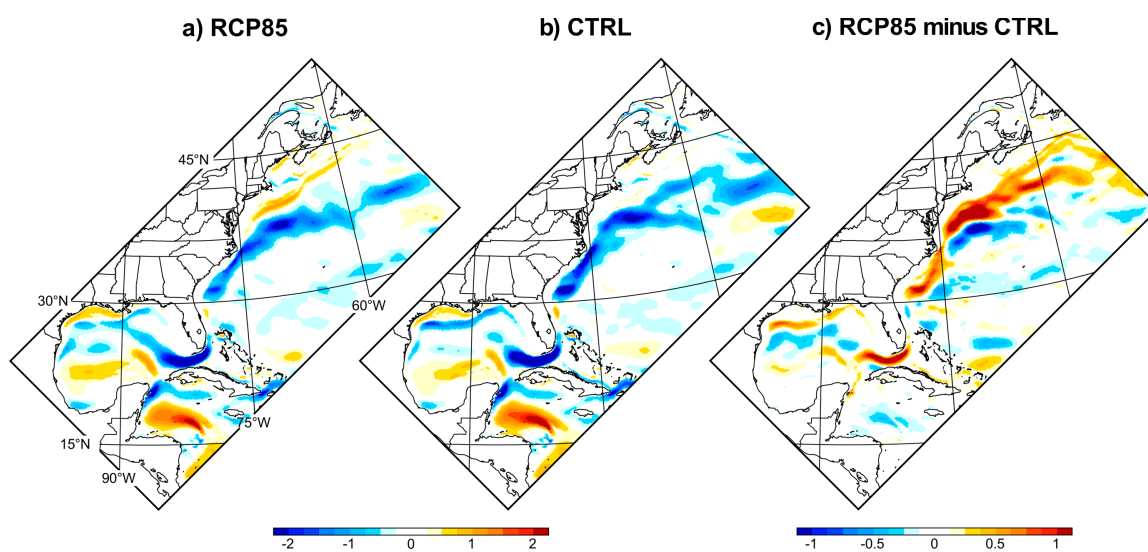


63

64 **Fig. 8.** (top) Maps of projected DJF sea surface temperature (color shadings) and surface
 65 current (vectors) responses, derived from a) ROMS downscaling and b) GFDL
 66 ESM2M simulations. For the ease of comparisons, the GFDL ESM2M responses
 67 were bilinearly interpolated to the ROMS grid, and the differences, a) minus b),
 68 are shown in c). (bottom) The same as the top but for the JJA.

69

70

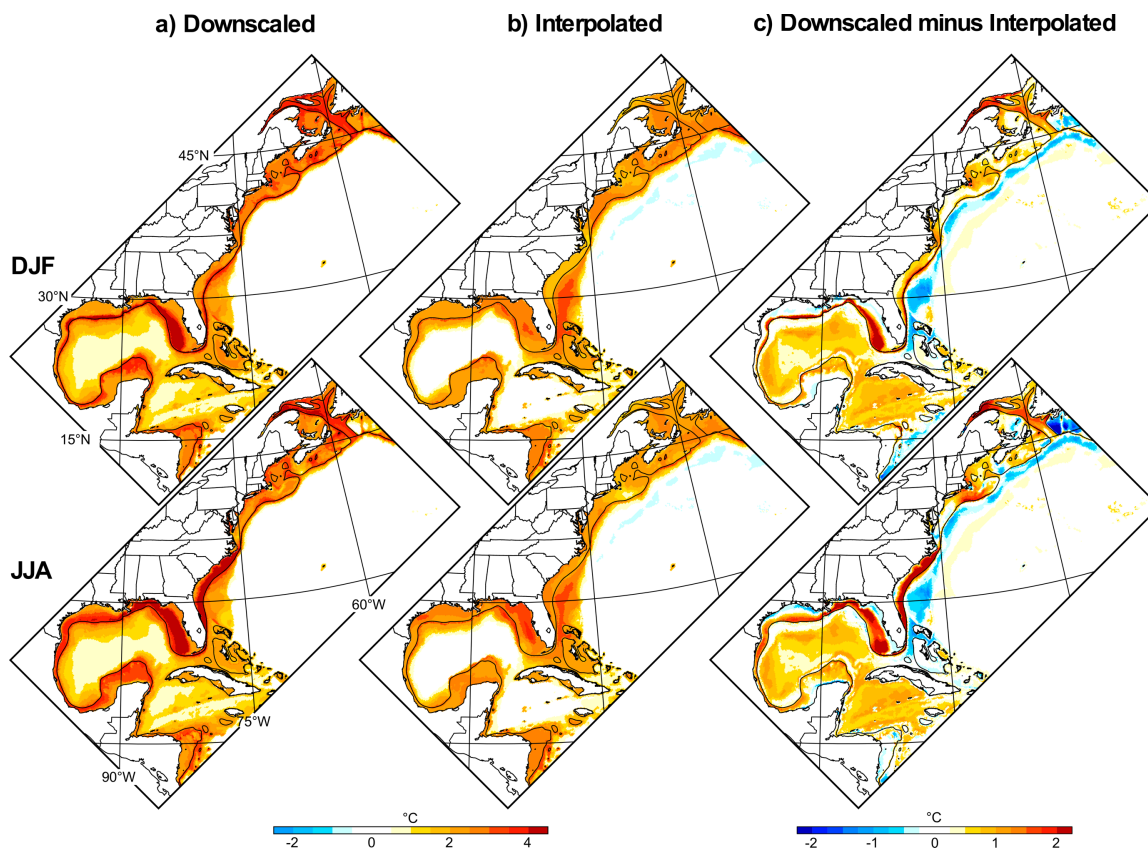


71

72 **Fig. 9.** Horizontal gradient maps of annually averaged sea surface height derived from a)
73 RCP85 and b) CTRL simulations. The differences, a) minus b), are shown in c).

74

75

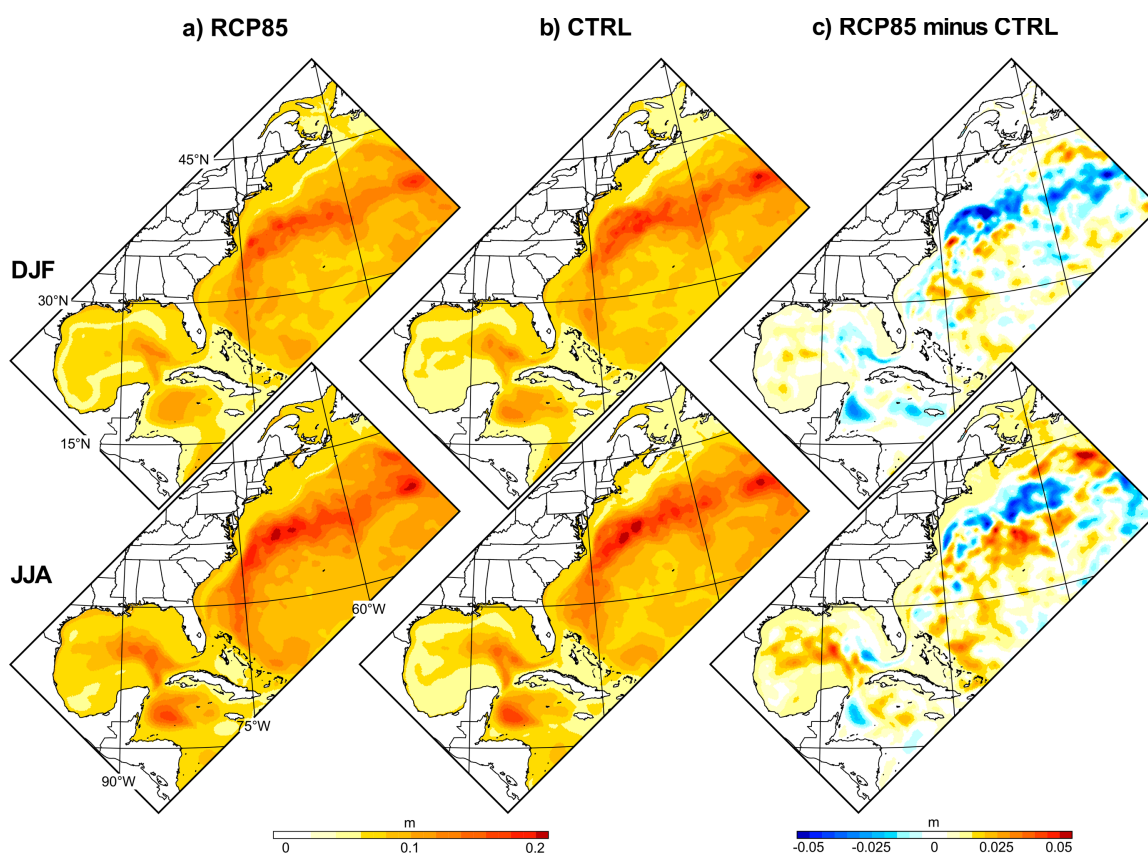


76

77 **Fig. 10.** (top) Maps of projected DJF ocean bottom temperature responses, derived from
 78 a) ROMS downscaling and b) GFDL ESM2M simulations. For the ease of
 79 comparisons, the GFDL ESM2M responses were bilinearly interpolated to the
 80 ROMS grid, and the differences, a) minus b), are shown in c). The grey contours
 81 in each map represent 200 m isobath. (bottom) The same as the top but for the
 82 JJA.

83

84

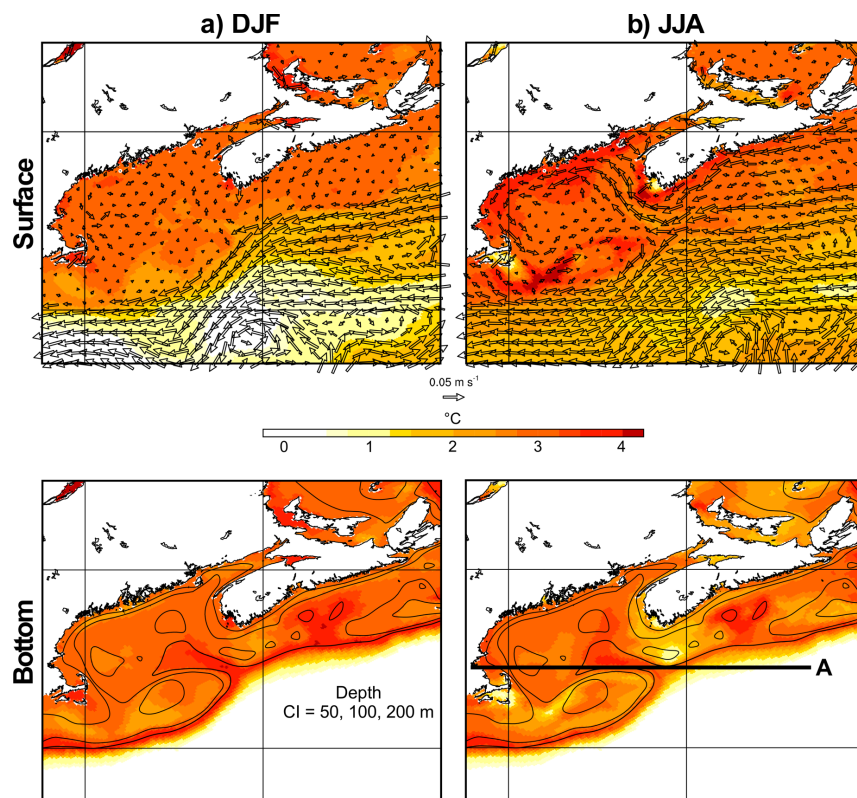


85

86 **Fig. 11.** (top) Maps of DJF high pass filtered transient ocean eddy statistics derived as sea
 87 surface height variance, $\overline{\eta'}^{1/2}$, in a) RCP85 and b) CTRL simulations. The
 88 differences, a) minus b), are shown in c). See text for the details of ocean eddy
 89 statistics estimation. (bottom) The same as the top but for the JJA.

90

91

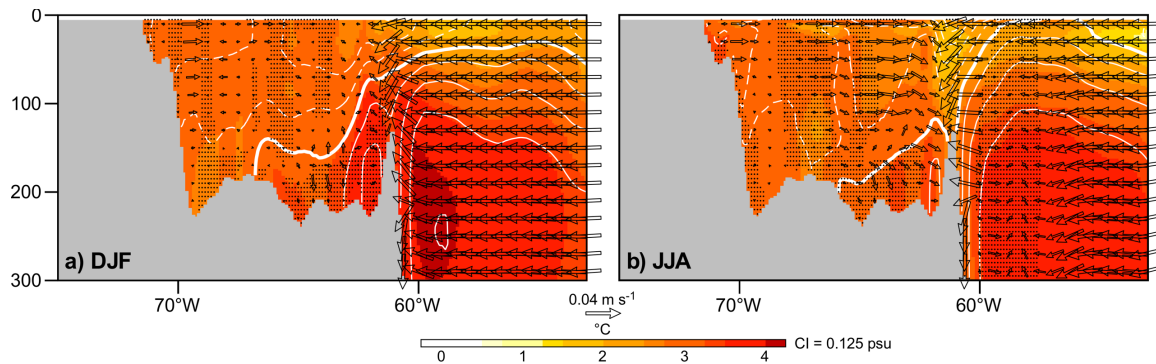


92

93 **Fig. 12.** (top) Maps of projected a) DJF and b) JJA temperature (color shadings) and
 94 current (vectors) responses at surface derived from ROMS downscaling exercise.
 95 (bottom) The same as the top but for the responses at ocean bottom. The thick
 96 black line A in the bottom panel represents the zonal cross section (42°N latitude)
 97 used in Fig. 13.

98

99

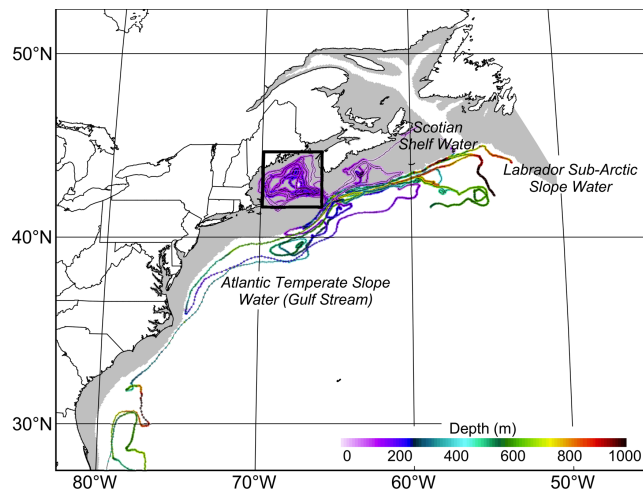


100

101 **Fig. 13.** Zonal cross section of projected a) DJF and b) JJA temperature (color shadings),
102 salinity (white contours), and zonal and vertical current (vectors) responses
103 derived from ROMS downscaling runs along the line A (see Fig. 12). The
104 anomalous northward meridional velocities are striped. Negative (zero) salinity
105 changes are denoted as dashed (thick) white contours.

106

107

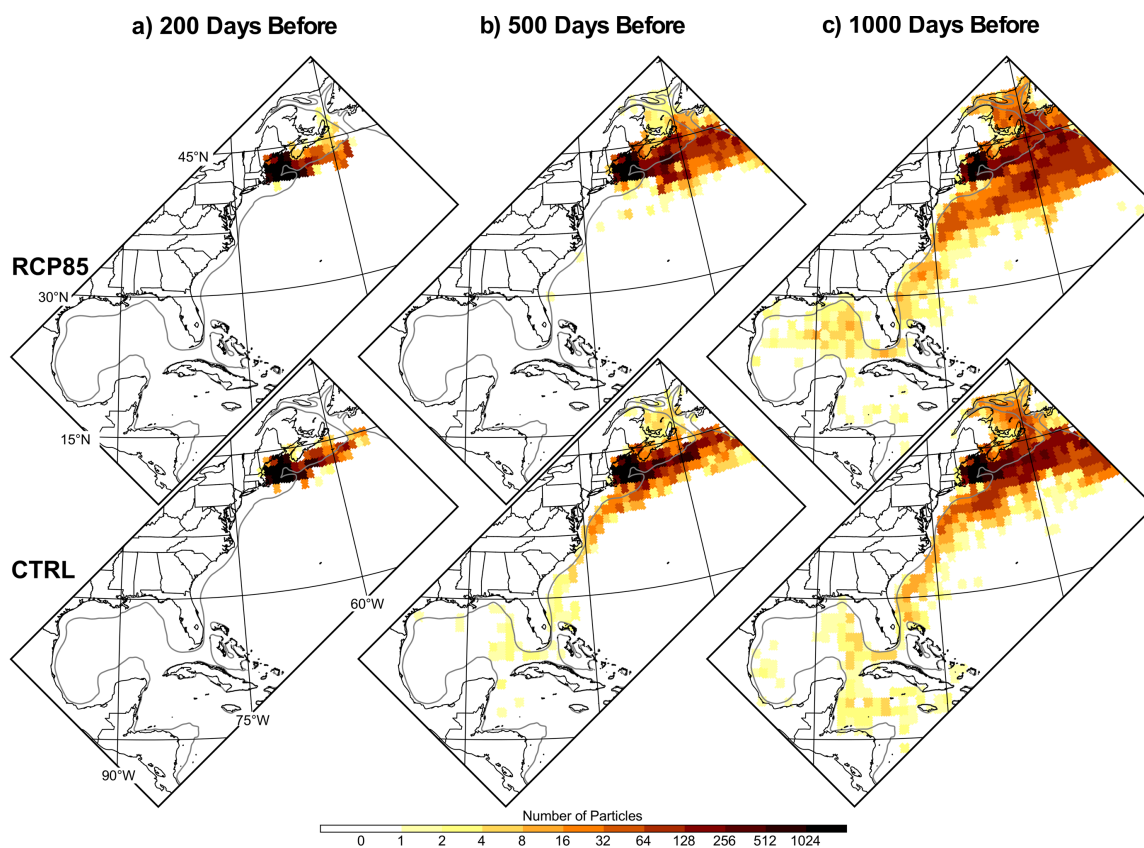


108

109 **Fig. 14.** The initial location map of 28,899 particles. The location is denoted as thick
110 black box representing the volumes spanning 41.63-44.61°N, 69.90-65.96°W,
111 and 145-327 m. The colored lines denote the three-dimensional backward
112 tracking of randomly chosen 20 particles located initially within the box for
113 1,000 days. The grey shaddings in each map represent the continental shelves
114 where the water depth is shallower than 200 m.

115

116

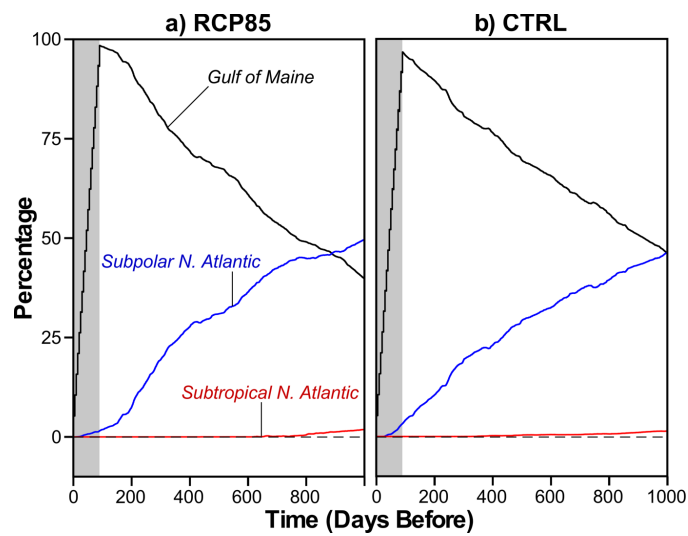


117

118 **Fig. 15.** (top) Maps of particle density at a) 200, b) 500, and c) 1,000 days before the
 119 initial time (June 2nd) derived from RCP85 run. (bottom) The same as the top but
 120 for the CTRL. See text for the details of backward particle tracking and particle
 121 density estimation. The grey contours in each map represent 200 m isobath.

122

123



124

125 **Fig. 16.** a) Percentage changes of particle densities over time, integrated over the Gulf of
 126 Maine (black line), subtropical N. Atlantic (red line), and subpolar N. Atlantic
 127 (blue line), derived from the RCP85 run. b) The same as a) but for the CTRL.

128